Title
Real-time tuning of MEMS gyro dynamics

Authors
Kim, DJ
M'Closkey, RT

Publication Date
2005-09-02

Peer reviewed

Real-Time Tuning of MEMS Gyro Dynamics

D. J. Kim and R. T. M'Closkey, *Member, IEEE*

***Abstract*— This paper reports real-time tuning of the JPL-Boeing micromachined vibratory rate sensor. The ideal sensor is designed to operate in a degenerate condition in which two modes of vibration have equal resonant frequencies. This condition achieves the best possible signal-to-noise ratio thereby maximizing sensor performance. A frequency split between the two modes, however, is inevitable in actual devices and leads to degraded performance. To modify the sensor dynamics to a desired condition, we have studied the bias potential effect on the sensor dynamics and successfully implemented a real-time tuning process via electrostatic forces to reduce the frequency split to less than 0.1 Hz when the nominal modal frequencies are near 4.4 kHz. A closed-loop identification method is employed for rapid and precise empirical frequency response estimates of the sensor dynamics. An LMI-based parameter estimation scheme produces an excellent fit of the model to the frequency response data and this enables the successful implementation of a steepest descent algorithm. Transformations for decoupling the MIMO sensor dynamics are also motivated and demonstrated.**

I. INTRODUCTION

The JPL-Boeing MEMS gyroscope, often referred to as the JPL microgyro, is a vibratory rate sensor. The sensor consists of a silicon micromachined plate suspended above a set of electrodes - two electrodes are used for sensing, two electrodes are used to apply electrostatic forces for actuation or "driving," and another two electrodes are used to apply bias potentials to the vibrating structure. A rigidly attached central post forms a "cloverleaf" assembly with the sensing and driving electrodes. The post strongly couples two lightly damped modes corresponding to rocking or tilting motion of the plate, referred to as the rocking modes, via a Coriolis term to render the device sensitive to rotational motion. The excitations of the sensor's lightly damped modes can be accomplished by applying a potential to the driving electrodes directly from a function generator or digital-to-analog converter (DAC). The sensing electrodes use a trans-impedance op-amp configuration to provide a buffered output voltage that is proportional to the rate of change of the gap between the electrodes and vibrating plate. More detailed information on the design and fabrication of the sensor may be found in [8].

This paper focuses on developing a real-time tuning process for the microgyro. Ideally, the sensor achieves the Coriolis coupling between two rocking modes of equal natural frequency. Manufacturing imperfections and package-induced stresses, however, are among various factors that make actual devices deviate from the ideal sensor dynamics and display an undesirable frequency split between the rocking modes. The tested device shows a frequency split of 5 Hz in the absence of bias potentials. This frequency split leads to degraded overall sensor performance since the degenerate modes are necessary for the sensor to achieve the largest signal-to-noise ratio (SNR). For example, as little as a 0.5 Hz difference in frequencies for these sensors produces a 20 dB degradation in SNR. If the split can be reduced below 0.1 Hz, the reduction in SNR is at most 5 dB - a tolerable figure. Therefore, post-fabrication tuning, preceded by an accurate estimate of the sensor dynamics, is an essential part of optimizing sensor performance.

This paper is organized as follows. Section II presents the analytical model for the sensor's rocking modes, generation of frequency response data, and formulation of parameter estimation problem using linear matrix inequalities (LMIs). Section III discusses the bias potential effect on the sensor dynamics, frequency split as a function of bias potentials, and real-time tuning results. Section IV concludes the paper.

II. GYRO MODEL AND PARAMETER ESTIMATION

A. Equation of Motion

The sensing electrodes of the JPL microgyro are not collocated with the driving electrodes. In the generalized sensor-fixed coordinates established by the sensing pick-offs denoted $x = [x_1, x_2]^T$, a linearized equation of motion describing the two lightly damped rocking modes can be written as

$$M\ddot{x} + C\dot{x} + \Omega S\dot{x} + Kx = Bu \tag{1}$$

In this model, M, C, and K are real, positive definite 2 x 2 mass, damping, and stiffness matrices, respectively, S is a skew-symmetric matrix modulated by the sensor angular rate of rotation Ω, B is a real, non-singular 2x2 matrix that specifies how forces applied by each drive electrode couple into the sensor-fixed coordinate frame, and $u = [u_1, u_2]^T$ is the electrostatic forces created by the potentials applied to the pair of drive electrodes. The frequency split between the rocking modes can be obtained from analyzing the generalized eigenvalues of M and K.

A dual version of (1) may be written in which the coordinates are established by the actuators (drive electrodes) as shown below

$$\begin{aligned} \tilde{M}\ddot{z} + \tilde{C}\dot{z} + \tilde{K}z &= u \\ x &= Rz \end{aligned} \tag{2}$$

This work was supported by NSF grant ECS-9985046 and the Boeing Aerospace Company via UC-MICRO 03-060.

D. J. Kim is a graduate research assistant with the Mechanical and Aerospace Engineering Department at the University of California, Los Angeles, CA 90095, USA (e-mail: dongj@seas.ucla.edu)

R. T. M'Closkey is an associate professor with the Mechanical and Aerospace Engineering Department at the University of California, Los Angeles, CA 90095, USA (corresponding author: 310-825-2909; e-mail: rtm@obsidian.seas.ucla.edu)

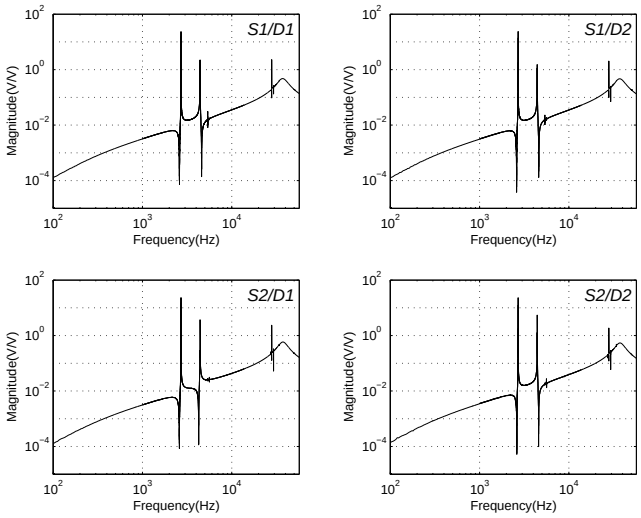

Fig. 1. Wideband frequency response of the sensor dynamics from a pair of driving electrodes (denoted D_1 and D_2) to a pair of sensing electrodes (denoted S_1 and S_1). The first lightly damped mode near 2.7 kHz is the linear translation mode. The next lightly damped mode is actually two rocking modes near 4.4 kHz that cannot be individually resolved in this scale. The remaining lightly damped modes above 5 kHz are other flexural modes of the sensor's elastic structure. The positive slope of the frequency response magnitude is caused by capacitive coupling between the drive and the sense electrodes. The attenuation above 35 kHz is attributed to the bandwidth of the signal conditioning amplifier.

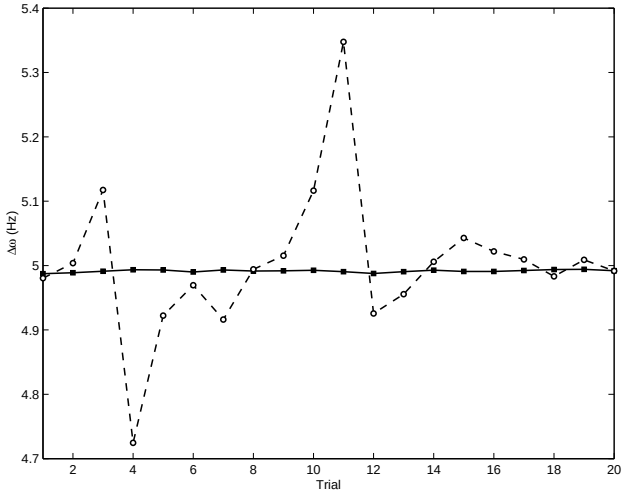

Fig. 2. Frequency split of identified ARX model (circle-dashed) vs. parametric model (square-solid). For 20 data sets acquired approximately 1 minute apart under the same condition, the ARX modeling scheme yields the standard deviation of $\Delta\omega$ over 0.1 Hz whereas the LMI-based parameter estimation scheme (described in Section II-C) produces the standard deviation of $\Delta\omega$ less than 0.01 Hz.

where R represents the transformation relating the drive electrode frame to the sense pick-off frame. The Coriolis term has been omitted from (2). Converting from one description to the other is a simple matter and which description is selected for modeling purposes depends upon the location of additional dynamics (at the sensor input or output) introduced by signal conditioning preamps, antialias filters, etc. It is obvious that (1) or (2) cannot fully explain the wide-band dynamics of the sensor shown in Fig. 1. In addition to the rocking modes near 4420 Hz, the sensor's elastic structure exhibits a linear translation mode near 2700 Hz and other flexural modes above 5000 Hz. Nevertheless, it is quite adequate to describe the sensor dynamics by (1) or (2) in a very narrow frequency band around the closely spaced rocking modes. Further information on the wide-band sensor dynamics may be found in [3].

B. Generation of Frequency Response Data

Our primary objective is to reduce the frequency split, denoted $\Delta\omega$, between the two modes of interest so an estimate of $\Delta\omega$ must be produced. We have employed an ARX modeling scheme [6] in the past to estimate various sensor parameters, however, we have observed that the standard deviation of $\Delta\omega$ is approximately 0.1 Hz as shown in Fig. 2, which is on the order of the resolution we require to obtain the full benefits of tuning (in order to make a fair comparison, both the ARX models and frequency domain models discussed in the sequel use approximately the same amount of data with the input power concentrated in a narrow band about the modes of interest). Furthermore, knowledge of the mass, stiffness, and damping matrices are valuable to the sensor designer and so it is useful to start with (1) as the basis for modeling instead of a more general difference equation employed in the ARX approach. In [3] we have developed a method for obtaining high quality frequency response data from these sensors. In brief, a closed-loop identification scheme is employed to reduce the sensor's inherent long settling time and the open-loop frequency response is recovered from the closed-loop data. In the following section, we will demonstrate that frequency response data is in fact ideally suited for identifying models like (1).

C. Parameter Estimation Problem

One approach for determining the (M, C, K, B) parameters in (1) is to minimize maximum modeling error across all frequency points represented in the data set,

$$\min_{\substack{M>0,C>0\\K>0,B\neq 0}} \max_k \overline{\sigma}(Z^{-1}(\omega_k)B - H_k) \qquad (3)$$

where $Z(\omega_k) = -M\omega_k^2 + K + j\omega_k C$, and H_k and ω_k are the k^{th} frequency response data point and frequency, respectively. This formulation is very much in the sprit of the classical Sanathanan-Koerner algorithm [7], although the positive definiteness constraints on M, C, and K complicate matters. The main objection to this formulation, however, is the undue emphasis placed on the frequencies and directions with large magnitude (relative to the other data points). This emphasis produces a poorer fit of the data at those frequencies which possess more modest gain. This has been recognized by other researchers and various ad hoc weighting schemes have been devised to distribute the error more fairly across the magnitude [1], [4]. The sensors

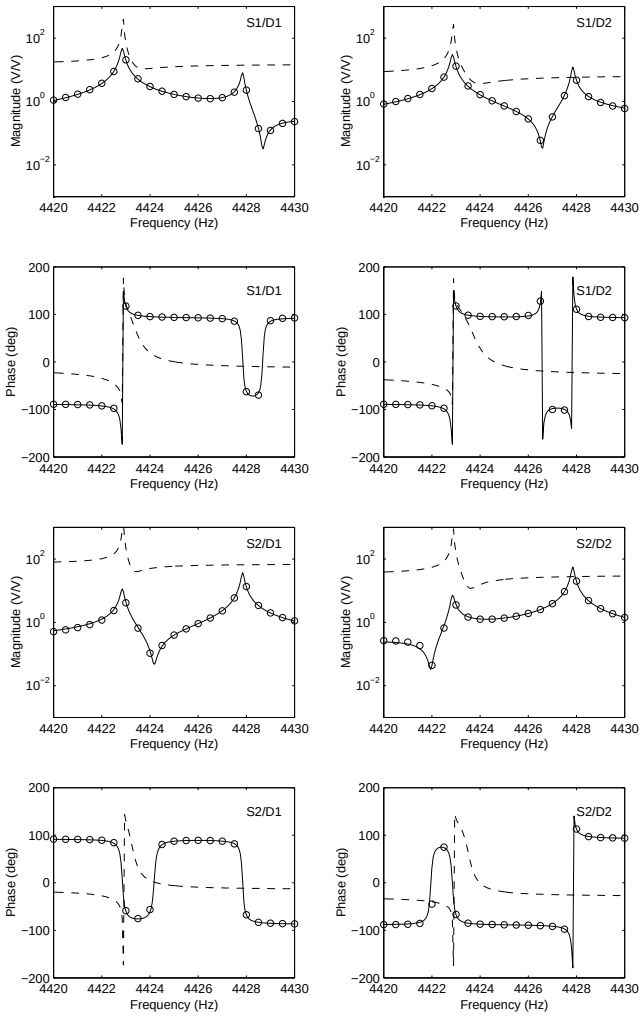

Fig. 3. Sensor's empirical frequency response (circle) vs. frequency response of the identified model assuming input perturbations (dashed) and output perturbations (solid). The sensing signals are passed through antialias filters to ensure that the feedback system is insensitive to the higher frequency dynamics. The drive signals are also passed through an identical set of filters to compensate the phase lag introduced by the antialias filters. While other phase perturbations remain uncertain, the model assuming output phase perturbations fits the empirical frequency response data very well whereas the model assuming input phase perturbations yields a very poor fit.

tested by our group represent an extreme case in which the frequency response can change by more than three orders of magnitude within a few Hertz. In this circumstance we have found that the following objective produces superior models,

$$\min_{\substack{M>0,C>0\\K>0,B\neq 0}} \max_k \overline{\sigma}(Z(\omega_k)H_k - B) \tag{4}$$

This problem has the fortune that the parameters appear affinely within the maximum singular value. Using the Schur complement formula, (4) may be rewritten as

$$\min_{\substack{\gamma>0,M>0\\C>0,K>0\\B\neq 0}} \max_k \underbrace{\begin{bmatrix} \gamma I & (Z(\omega_k)H_k - B)^* \\ Z(\omega_k)H_k - B & \gamma I \end{bmatrix}}_{=:J_k} > 0. \tag{5}$$

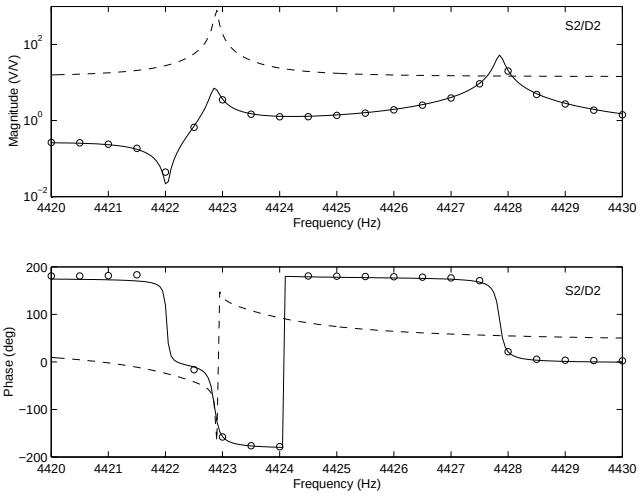

Fig. 4. Sensor's empirical frequency response (circle) vs. frequency response of the identified model assuming input perturbations (dashed) and output perturbations (solid). In this case, the drive signals are not re-sampled. Only a single channel from D2 to S2 is shown. The model assuming output phase perturbations still estimates the empirical frequency response very well and extra 90 degrees of phase lag are observed when comparing to Fig. 3

When there are N frequency response data points available, this optimization can be stated as the standard generalized eigenvalue problem (GEVP) [2],

$$\begin{aligned} \text{minimize:} \quad & \gamma \\ \text{subject to:} \quad & \gamma > 0, M > 0, C > 0, K > 0 \\ & J_k > 0 \text{ for } k = 1 \ldots N \end{aligned} \tag{6}$$

that can be solved by several commercially available software packages (Matlab's LMI Control Toolbox is used in this paper). In our formulation, the (1,1) element of the mass matrix is normalized to 1 without loss of generality. At this point there is nothing that recommends either form of the model. The choice becomes critical, however, when additional dynamics at the sensor input or output are included. Let us first consider dynamics at the output of the sensor, denoted H_{out}, that can be used to capture the effects of the sensor's signal conditioning preamplifiers and antialias filters.

In this case the error to be minimized is $\overline{\sigma}(H\tilde{Z} - H_{out}R)$ where $\tilde{Z}(\omega_k) = -\tilde{M}\omega_k^2 + \tilde{K} + j\omega_k\tilde{C}$. The specification of a general form for H_{out}, however, will render the computation non-convex. In the present case though we are interested in a narrow band of frequencies where the modes are located. It is quite reasonable to assume that any additional dynamics at the sensor output can be modeled by an FIR filter. In fact, we often represent these extra dynamics as constant magnitude and phase perturbations. For example, our experiments use eight pole butterworth antialias filters with 20 kHz corner frequencies that experience a 0.2 degree change in phase and essentially a 0 dB change in magnitude in a 10 Hz band containing the two modes of interest. In this case, we can combine $H_{out}R$ into a single, fixed complex matrix $\hat{R}$. This approach is pursued here and leads to the

optimization in (5) where

$$J_k = \begin{bmatrix} \gamma I & (H_k\tilde{Z}(\omega_k) - \hat{R})^* \\ H_k\tilde{Z}(\omega_k) - \hat{R} & \gamma I \end{bmatrix}, \qquad (7)$$

and where $\tilde{M} > 0$, $\tilde{C} > 0$, $\tilde{K} > 0$, and $\hat{R} \in \mathbb{C}^{2\times 2}$.

An analogous argument can be made for dynamic perturbations acting at the sensor input (denoted H_{in}) and in this case we use (1) as the basis for modeling the sensor dynamics. The error is $\overline{\sigma}(ZH - BH_{in})$ and if an assumption can be made concerning the nearly constant magnitude and phase of H_{in} in the tested frequency band, then BH_{in} can be replaced with a single, fixed complex matrix whose elements are to be determined in the optimization. In this case, we replace J_k in (5) with

$$J_k = \begin{bmatrix} \gamma I & (Z(\omega_k)H_k - \hat{B})^* \\ Z(\omega_k)H_k - \hat{B} & \gamma I \end{bmatrix}, \qquad (8)$$

and where $M > 0$, $C > 0$, $K > 0$, and $\hat{B} \in \mathbb{C}^{2\times 2}$.

Currently, there is no graceful way to handle simultaneous input and output perturbations: if an input perturbation is present and we use (7) for obtaining the model parameters, the perturbation becomes "buried" in the $H_k\tilde{Z}(\omega_k)$ product and cannot be compensated by the additional freedom present in $\hat{R}$. Similarly, an output perturbation in (8) is obscured by the $Z(\omega_k)H_k$ product and cannot be compensated by $\hat{B}$. These claims are supported by our optimization results using real frequency response data. Fig. 3 compares the results of fitting the model using (7) and (8). The same termination criteria are used in each case. It is quite evident that the model fit assuming input perturbations is extremely poor while the formulation that assumes output perturbations provides a very good fit. The matrix from the latter case is

$$\begin{aligned} \hat{R} &= \begin{bmatrix} -20.47 & -34.30 \\ 51.85 & -65.25 \end{bmatrix} + j \begin{bmatrix} -0.65 & -1.37 \\ 1.87 & -2.23 \end{bmatrix} \\ &\approx \begin{bmatrix} e^{j\theta_1} & 0 \\ 0 & e^{j\theta_2} \end{bmatrix} \begin{bmatrix} -20.48 & -34.33 \\ 51.89 & -65.29 \end{bmatrix}, \end{aligned} \qquad (9)$$

which demonstrates that the channels' phases are perturbed by $\theta_1 = 2.01$ degrees and $\theta_2 = 2.13$ degrees. This is consistent with measurements made at other frequencies. The data used in this example had the effect of the antialias filters removed by re-sampling the excitation signals with an identical bank of filters (so no relative delay is introduced). If we remove the re-sampling then the data contain additional lag. In this case, the formulation assuming output perturbations still produces a model that fits the data extremely well as shown in Fig. 4.

III. ELECTRONIC TUNING

A. Bias Potential Effect on Sensor Dynamics

To illustrate the bias potential effect on the sensor dynamics, a single degree-of-freedom (DOF) system is introduced. For the single DOF system shown in Fig. 5, the electrostatic force F_e between two capacitor plates is defined as

$$F_e = -\varepsilon_0 A V_b^2 / 2d^2 \qquad (10)$$

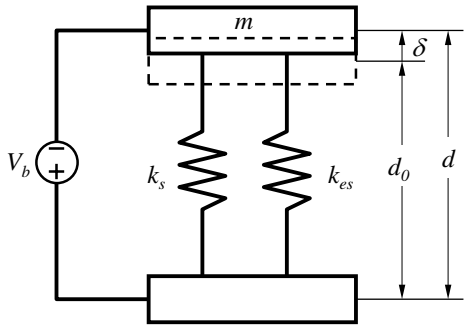

Fig. 5. Bias potential effect on a single DOF system. When the mass m moves a small displacement d from the equilibrium position, the equivalent spring constant becomes $k_{eq} = k_s + k_{es}$.

where ε_0, A, V_b, and d are the permittivity constant, electrode area, bias potential, and the gap distance between the plates, respectively. Let as shown, where d_0 and δ are the equilibrium gap distance between the plates and small displacement from d_0, respectively. A linear approximation of (10) yields a linearized electrostatic spring constant k_{es} as

$$k_{es} = -\varepsilon_0 A V_b^2 / d_0^3 \qquad (11)$$

where the negative sign implies that k_{es} introduces a softening spring effect. The equivalent stiffness k_{eq} is then computed as the sum of the mechanical stiffness k_s of the system and the electrostatic stiffness k_{es} created by the applied bias voltage. Hence, the variation of bias potential can shift the resonant frequency of the system. By analogy with the single DOF case, the overall stiffness matrix for a multiple DOF system can be represented as the sum of the mechanical stiffness matrix and the electrostatic stiffness matrix created by the applied bias potential. Since the JPL microgyro is equipped with two bias electrodes, the overall stiffness matrix of the sensor dynamics K_{total} becomes

$$K_{total} = K_0 + K_B(B_1, B_2) \qquad (12)$$

where K_0 is the elastic stiffness matrix of the system, and K_B is the symmetric electrostatic stiffness matrix created by the bias potentials B_1 and B_2. Therefore, we can control $\Delta\omega$ between the two rocking modes by varying B_1 and B_2.

B. Real-Time Tuning

It can be shown that $\Delta\omega^2$ is an analytic function of bias potentials and that any minimum is global. Indeed, the contours in Fig. 6 were generated by exhaustive testing of the sensor at a grid of bias potentials; empirical frequency response data is generated at every pair of potentials and then a model is fit using (6) and (7). The frequency split is extracted from the models and then used to create Fig. 6. The desirable properties of $\Delta\omega^2$ as well as the excellent models obtained by fitting the frequency response data suggest that a robust method for reducing $\Delta\omega$ below some tolerance is possible. This is indeed the case and we have employed the method of steepest descent [5] for

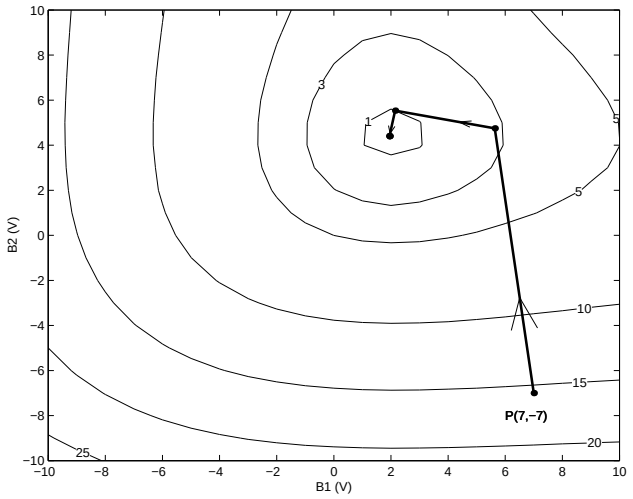

Fig. 6. Contour plot of $\Delta\omega$ as a function of B_1 and B_2. The plot is based on frequency split data for B_1 and B_2 from -10 V to 10 V with a step of 1 V. Tuning from (B_1, B_2) = (-7 V, -7 V) with $\Delta\omega = 15.16$ Hz reaches $(5.63V, 4.75V)$ with $\Delta\omega = 2.81$ Hz after the 1st iteration and (2.14 V, 5.54 V) with $\Delta\omega = 0.91$Hz after the 2nd iteration. Finally, the process stops at (1.95 V, 4.40 V) with $\Delta\omega = 0.045$ Hz.

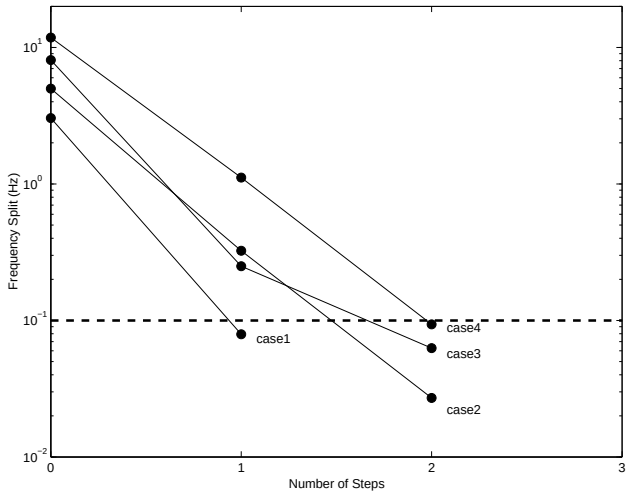

Fig. 7. Tuning from different starting bias points. **Case 1:** (0 V, 2 V) with $\Delta\omega$ = 3.04 Hz $\rightarrow$ (1.98 V, 4.33 V) with $\Delta\omega$ = 0.079 Hz. **Case 2:** (0 V, 0 V) with $\Delta\omega$ = 4.99 Hz $\rightarrow$ (1.70 V, 4.58 V) with $\Delta\omega$ = 0.32 Hz $\rightarrow$ (1.99 V, 4.41 V) with $\Delta\omega$ = 0.027 Hz. **Case 3:** (-5 V, 5 V)with $\Delta\omega$ = 8.09 Hz $\rightarrow$ (2.08 V, 4.71 V) with $\Delta\omega$ = 0.25 Hz $\rightarrow$ (1.93 V, 4.40 V) with $\Delta\omega$ = 0.063 Hz. **Case 4:** (4 V, -5 V) with $\Delta\omega$ = 11.82 Hz $\rightarrow$ (3.31 V, 4.59 V) with $\Delta\omega$ = 1.11 Hz $\rightarrow$ (2.11 V, 4.48 V) with $\Delta\omega$ = 0.094 Hz.

this purpose. Define $\Delta\omega^2 = f(B_1, B_2)$, then the iterative algorithm can be written as

$$\vec{B}_{k+1} = \vec{B}_k - \alpha_k \nabla f(\vec{B}_k) \tag{13}$$

where $\vec{B} = [B_1, B_2]^T$, α_k is a nonsingular scalar minimizing $f(\vec{B}_k - \alpha_k \nabla f(\vec{B}_k))$. The gradient in (13) is computed with the central difference approximations as

$$\begin{aligned} \frac{\partial f(B_1, B2)}{\partial B_1} &\approx \frac{f(B_1 + h, B_2) - f(B_1 - h, B_2)}{2h} \\ \frac{\partial f(B_1, B2)}{\partial B_2} &\approx \frac{f(B_1, B_2 + h) - f(B_1, B_2 - h)}{2h} \end{aligned} \tag{14}$$

where h is chosen to be 0.1V and is weighted by $\Delta\omega$ when $\Delta\omega < 1$ Hz for better estimation of the local gradient. Next, a Fibonacci line search [5] is used to determine the minimum along the gradient direction within set limits on the bias electrode potentials (10 V in our case). The iteration stops once the dynamics are nearly degenerate: the modes are tuned to within 0.1 Hz to obtain the highest SNR during sensor operation. Different tuning paths from four different starting points are shown in Fig. 7. The tuning process is evidently convergent in searching for the optimum set of bias potentials. Fig. 8 shows the frequency response data and the identified models during a typical tuning run.

C. Channel Decoupling

Even though the sensor is tuned there may still exist a large amount of cross channel coupling. This is evident in Fig. 8 where the off-diagonal frequency response magnitudes are comparable to the diagonal terms. This degree of coupling is undesirable because during operation one channel is driven to a constant amplitude sinusoidal response at the tuned resonant frequency while the other channel is regulated to zero (ideally) with a high gain loop (for example, see [3] for a description as to why vibratory rate sensors are operated in this manner). The threat from large cross channel coupling comes from the fact that the high gain channel can be saturated. Reducing the channel coupling, that is creating a sensor with essentially a diagonal transfer function, eliminates this potential for saturation. Decoupling can be achieved by determining two 2x2 constant-gain input and output transformations, denoted T_{in} and T_{out} respectively, that render diagonally dominant sensor dynamics. The sensor's mass and stiffness matrices may be simultaneously diagonalized as $V^T M V$ and $V^T K V$ where V is the matrix whose columns are the generalized eigenvectors of M and K. If we let $z = Vy$ and multiply the both sides by V^T, (2) becomes

$$V^T \tilde{M} V \ddot{y} + V^T \tilde{C} V \dot{y} + V^T \tilde{K} V y = V^T u \tag{15}$$

and (15) implies $T_{out} = (RV)^{-1}$ and $T_{in} = V^{-T}$. Fig. 9 illustrates the decoupled sensor dynamics. The modes are tuned to within 0.1 Hz and the sensor's empirical frequency response has a 0.1 Hz frequency resolution over the displayed range. It is evident that the transformations decouple the rocking modes into separate channels and the peak gain in the diagonal channels is higher than the peak gain in the off diagonal channels by an order of magnitude. The condition numbers of T_{in} and T_{out} are 1.39 and 1.42, respectively, indicating that any modeling error is not exacerbated by the transformations.

IV. CONCLUSIONS

We have presented a real-time tuning scheme for the JPL microgyro. We have successfully implemented the tuning process to achieve the frequency split less than 0.1 Hz. One

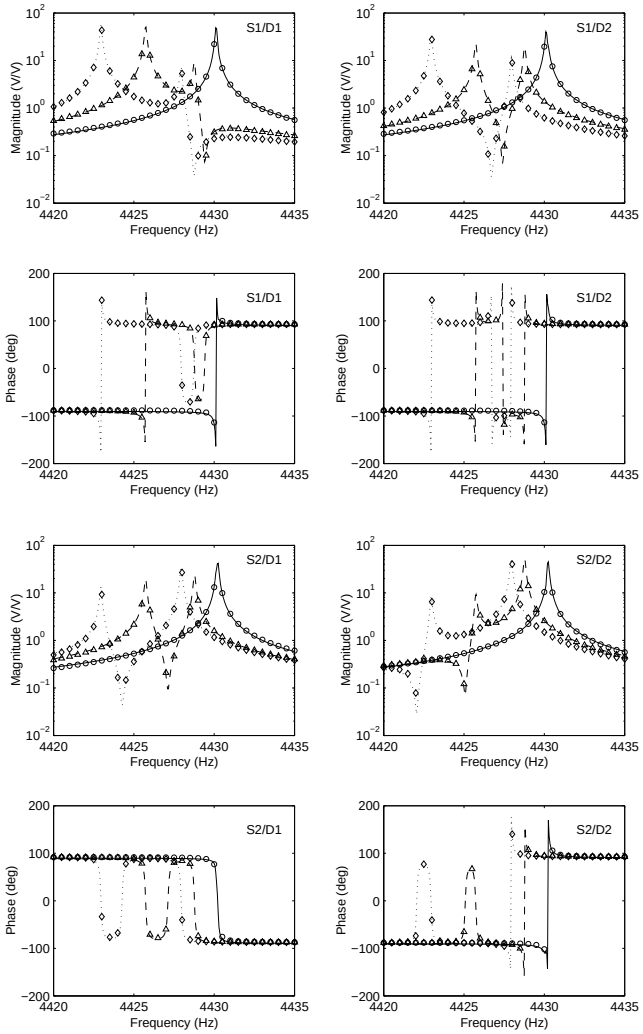

Fig. 8. Empirical frequency response and the identified models during a typical tuning run; diamonds, triangles, and, circles are empirical frequency response data corresponding to the starting, intermediate, and final set of biases with a frequency split of 5 Hz, 3 Hz, and 0.08 Hz, respectively; and dotted, dashed, and solid traces are the identified models.

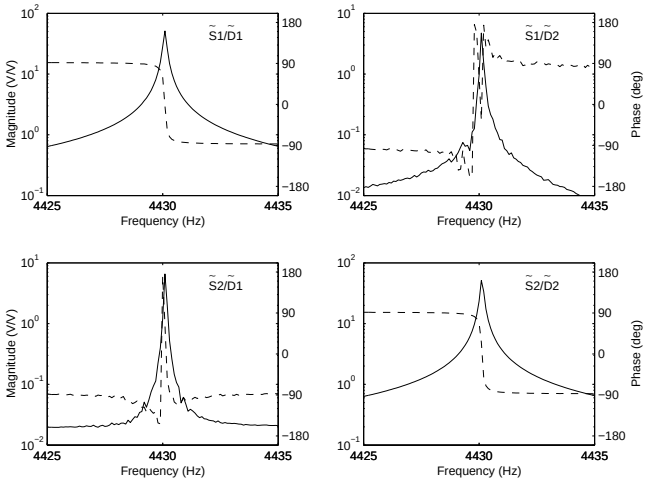

Fig. 9. Empirical frequency response estimate of decoupled sensor dynamics (the decoupling transformations are applied directly to the frequency response data generated with a 0.1 Hz resolution). The magnitude and phase are the solid and dotted traces, respectively. The virtual sensing electrodes and driving electrodes, denoted $\tilde{S}$ and $\tilde{D}$, are related to the native electrodes by $\tilde{S} = T_{out} S$ and $D = T_{in} \tilde{D}$, respectively. The dominant diagonal channels display decoupled sensor dynamics.

appealing aspect of post fabrication tuning is that it is a very cost effective method to improve sensor performance. The tuning process discussed in this paper has a great practicality since it can be applied to many rate gyros with a wide range of dynamic responses.

V. ACKNOWLEDGMENTS

We would like to thank Dorian Chanlloner of Boeing Satellite Systems for his support of our research program.

REFERENCES

[1] Bayard, D. S., "High-order wide-band frequency domain identification using composite curve fitting," *Proceedings of the 1992 American Control Conference*, Chicago, IL, Jun. 1992, vol. 4, pp. 3181-3185.

[2] Boyd, S., Ghaoui, L. E., Feron, E., and Balakrishnan, V., *Linear matrix inequalities in systems and control theory*. Philadelphia, PA: SIAM, 1994, pp. 9-12.

[3] Chen, Y.-C. and M'Closkey, R. T., "Closed-loop identification of a micro-sensor," *Proceedings of the 42nd IEEE Conference on Decision and Control*, Maui, Hawaii, Dec. 2003, pp. 2632-2637.

[4] [4] Fisher, D., Jue, D., Packard, A., and Poolla, K., "On the identification of high-order lightly-damped multivariable systems," Proceedings of the 1999 American Control Conference, San Diego, CA, Jun. 1999, vol.2, pp.848-853.

[5] Luenberger, D. G., *Linear and nonlinear programming. 2nd ed. Reading*, MA: Addison-Wesley Publishing Co., 1989, ch. 7.

[6] M'Closkey, R. T., Gibson, S., and Hui, J., "System identification of a MEMS gyroscope," *Journal of Dynamic Systems, Measurement, and Control, Transactions of the ASME*, Jun. 2001, vol. 123, No. 2, pp.201-210.

[7] Sanathanan, C. K., and Koerner, J., "Transfer function synthesis as a ratio of two complex polynomial," *IEEE Trans. Automatic Control*, pp. 56-58, Jan.1963.

[8] Tang, T. K., Gutierrez, R. C., Wilcox, J. Z., Stell, C., Vorperian, V., Calvet, R., Li, W. J., Charkaborty, I., Bartman, R., and Kaiser, W. J., "Silicon bulk micromachined vibratory gyroscope," *Solid-State Sensor and Actuator Workshop*, Hilton Head, SC, pp. 288-93, 1996.